

F 6 Drug delivery in blood

D. A. Fedosov, K. Müller, and G. Gompper

Institute of Complex Systems

Forschungszentrum Jülich GmbH

Contents

1	Introduction	2
1.1	Blood	2
1.2	Blood cells	2
1.3	Drug delivery	3
2	Methods and models	4
2.1	Blood cells and suspended particles	4
2.2	Simulation setup and definitions	6
3	Results	7
3.1	Particle margination	7
3.2	Dependence of margination on particle size	9
3.3	Dependence of margination on vessel size	11
3.4	Dependence of margination on particle shape	11
4	Discussion and conclusions	12
A	Dissipative particle dynamics	13

1 Introduction

1.1 Blood

Blood is circulated around the entire body performing a number of physiological functions. Its main functions are the transport of oxygen and nutrients to cells of the body, removal of waste products such as carbon dioxide and urea, and circulation of molecules and cells which mediate the organism's defense and immune response and play a fundamental role in the tissue repair process. Abnormal blood flow is often correlated with a broad range of disorders and diseases which include, for instance, hypertension, anemia, atherosclerosis, malaria, and thrombosis. Understanding the rheological properties and dynamics of blood cells and blood flow is crucial for many biomedical and bioengineering applications. Examples include the development of blood substitutes, the design of blood flow assisting devices, and drug delivery. In addition, understanding of vital blood related processes in health and disease may aid in the development of new effective treatments.

Blood is a physiological fluid that consists of erythrocytes or red blood cells (RBCs), leukocytes or white blood cells (WBCs), thrombocytes or platelets, and plasma containing various molecules and ions. RBCs constitute about 45% of the total blood volume, WBCs around 0.7%, and the rest is taken up by blood plasma and its substances. One microliter of blood contains about 5×10^6 RBCs, roughly 5000 WBCs, and approximately 2.5×10^5 platelets.

1.2 Blood cells

Figure 1 shows a scanning electron micrograph of blood cells. Human RBCs have a relatively

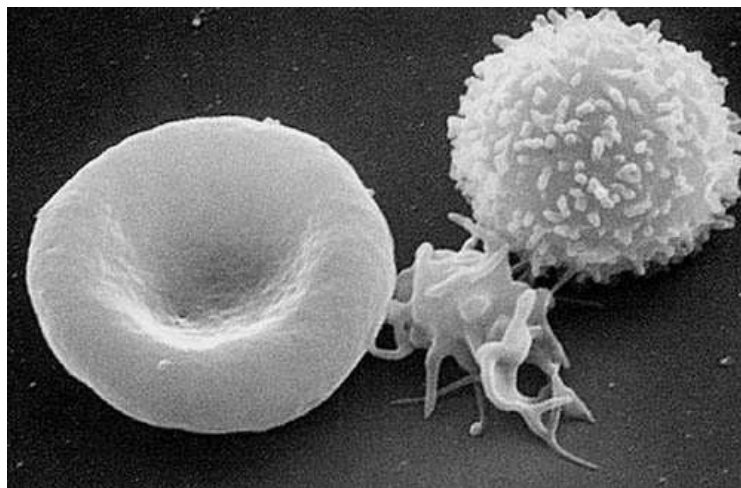


Fig. 1: A scanning electron micrograph of blood cells. From left to right: human erythrocyte, thrombocyte (platelet), leukocyte.

simple structure in comparison to other cells. RBCs resemble biconcave disks with an average diameter of approximately $8 \mu\text{m}$ and contain a viscous cytosol enclosed by a membrane. A RBC membrane consists of a lipid bilayer with an attached cytoskeleton formed by a network of the spectrin proteins linked by short filaments of actin. At the stage of the RBC formation, the nucleus and other organelles that are generally present in other eukaryotic cells are ejected, leaving behind a relatively homogeneous cytoplasm and no inner cytoskeleton. RBC cytoplasm

is a hemoglobin rich solution, which is able to bind oxygen. Therefore, the main RBC function is oxygen supply and delivery to body tissues. RBCs are extremely deformable and can pass through capillaries with a diameter several times smaller than the RBC size.

In comparison to RBCs, WBCs are spherical in shape with a diameter between 7 μm and 20 μm . WBCs have one or multiple nuclei and are stiffer than RBCs. However, WBCs are also able to undergo significant deformation when entering the smallest blood capillaries. WBCs are an important part of the body's immune system. They protect the body against invading bacteria, parasites, and viruses by killing these microorganisms through phagocytosis ingestion and other antigen-specific cytotoxic mechanisms. There exist different types of leukocytes (e.g., neutrophils, eosinophils, basophils, monocytes, and lymphocytes), each of which is designed to fight a specific type of infection. WBCs may adhere to the vascular endothelium, which is important for their physiological function in the immune response.

1.3 Drug delivery

The use of targeted micro- and nano-carriers for the delivery of imaging agents and drugs provides a promising strategy for early detection and treatment of diseases, e.g., of cancer [1, 2]. However, the design of particles carrying different contrast agents and drugs as well as their physical delivery are very challenging tasks. Micro- and nano-particle fabrication, which needs to address several issues such as bio-compatibility, durability, binding to specific targets, and the ability of controlled release, has been strongly advanced in recent years [3, 4, 5]. Nevertheless, the development of efficient strategies for the delivery of carriers, including their distribution in the organism following systemic administration [6] and their transport through biological barriers [6, 7, 8] (e.g., microvascular walls, interstitial space, and cell membranes), requires a much more detailed understanding of the relevant physical and biological mechanisms [2, 6, 9, 10].

Successful delivery of micro- and nano-carriers strongly depends on their efficient binding to specific targeted sites. Consequently, the distribution of carriers within vessel cross-sections plays an important role, since binding of carriers is only possible in case of direct particle-wall interactions. The cross-sectional distribution of micro- and nano-particles depends on several relevant parameters, which concern blood flow properties (such as flow rate, RBC deformability, and hematocrit – the volume fraction of RBCs), vessel size, and particle characteristics (such as size, shape, and deformability). The migration of various suspended particles or cells toward walls in blood flow, which is often referred to as *margination*, has been observed experimentally for white blood cells [11, 12], platelets [13], and rigid micro-particles [14, 15]. Particle margination is mediated by RBCs, which migrate to the vessel center due to hydrodynamic interactions with the walls (called lift force) [16, 17] leading to a RBC-free layer near the walls. More precisely, the occurrence of margination is a consequence of the competition between lift forces on RBCs and suspended particles, and their interactions in flow [18]. However, the dependence of margination efficiency on particle size and shape remains largely unexplored so far.

The role of particle size and shape in the efficient delivery is a multi-faceted problem. Large enough particles with a characteristic diameter (D_p) greater than about 4 μm may become trapped in the smallest capillaries of the body [19]. In addition, recent experiments suggest that large particles with $D_p \gtrsim 3 \mu\text{m}$ are subject to an enhanced phagocytosis [20]. However, recent microfluidic experiments [21] have shown that spheres with the size of 2 μm show a significantly higher adhesion density than particles with a size of 200 nm and 500 nm. Other experiments [22] indicate that liposomes with $D_p < 70 \text{ nm}$ and $D_p > 300 \text{ nm}$ have shorter

circulation times than those having an intermediate size of $D_p \approx 150 - 200$ nm. Furthermore, nano-particles with a size below $20 - 30$ nm are rapidly excreted through the kidneys [23]. Adhesion of different particles has been studied experimentally [24, 25] and theoretically [26, 27], with the result that oblate ellipsoids are subject to stronger adhesion than spheres with the same volume. To better understand the adhesion potential of micro- and nano-particles, a quantitative description of particle margination under realistic blood flow conditions is required.

In this chapter, we investigate the role of particle size and shape on the margination efficiency, and therefore on their adhesion potential. Several sizes ranging from about hundred nanometers to a few micrometers and two different shapes (circular and elliptical) are considered. The margination of micro- and nano-particles is studied numerically for a wide range of hematocrit values, vessel sizes, and flow rates using a two-dimensional (2D) model. Our results indicate that large particles possess a larger probability of being margined than small particles. As the particle size becomes very small (less than about $100 - 200$ nm), the particle distribution within vessel cross-section can be described well by the plasma volume around flowing RBCs. Furthermore, circular particles marginate better than ellipses, however the adhesion efficiency of elliptical particles is expected to be superior in comparison to that of circles due to their smaller adhesion area.

2 Methods and models

To represent fluid flow, the dissipative particle dynamics (DPD) method [28, 29] is employed. DPD is a mesoscopic particle-based simulation approach which properly captures hydrodynamics often described by the incompressible Navier-Stokes equation. Detailed description of the DPD method can be found in Appendix A.

2.1 Blood cells and suspended particles

To study margination of micro- and nano-particles in blood flow, it is sufficient to model only RBCs, since volume fraction of the other blood cells is negligible in comparison to the volume fraction of RBCs. The RBC volume fraction is referred to as hematocrit H_t . In 2D, RBCs are modeled by a collection of $N_v = 50$ particles connected by $N_s = N_v$ springs [30] with the potential [31]

$$V_{spring} = \sum_{j \in 1 \dots N_s} \left[\frac{k_B T l_m (3x_j^2 - 2x_j^3)}{4p(1 - x_j)} + \frac{k_p}{l_j} \right], \quad (1)$$

where l_j is the length of the spring j , l_m is the maximum spring extension, $x_j = l_j/l_m$, p is the persistence length, $k_B T$ is the energy unit, and k_p is the spring constant. A balance between the two force terms in Eq. (1) determines a non-zero equilibrium spring length l_0 . The cell model also incorporates a bending energy between two consecutive springs given by

$$V_{bend} = \sum_{j \in 1 \dots N_v} k_b [1 - \cos(\theta_j)], \quad (2)$$

where k_b is the bending constant and θ_j is the instantaneous angle between two adjacent springs having the common vertex j . In addition, a constraint to maintain a constant cell area is imposed on each cell by the potential

$$V_{area} = k_a \frac{(A - A_0)^2}{2A_0}, \quad (3)$$

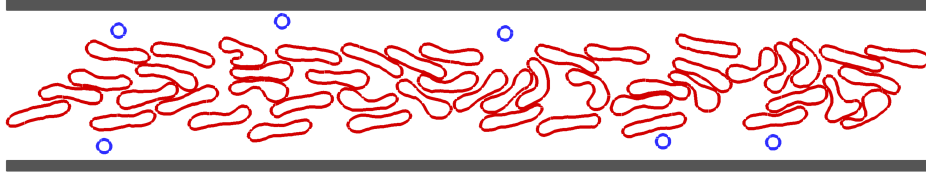


Fig. 2: Snapshot of blood flow in a micro-channel in 2D. RBCs are colored in red and suspended particles in blue. Simulation conditions correspond to $H_t = 0.3$ and $\dot{\gamma}^* \approx 29.3$.

where k_a is the area constraint coefficient, A is the instantaneous RBC area, and A_0 is the specified (target) area.

The RBC diameter is chosen to be $D_r \equiv L_0/\pi$, where $L_0 = N_s l_0$ is the cell perimeter. For comparison in physical units, typical value for healthy RBCs is $D_r = 6.1 \mu\text{m}$. The combination of A_0 and L_0 determines the shape of a RBC which is characterized by the reduced area $A^* = 4A_0/(\pi D_r^2) = 0.46$. The RBC equilibrium spring length is $l_0 = 0.063D_r$ and $l_m/l_0 = 2.2$. In all simulations $k_b = 50 k_B T$ for RBCs. The other important non-dimensional number, which characterizes the ratio of RBC elasticity to bending rigidity, is $\alpha = Y D_r^2/\kappa$, where $Y = (-\partial^2 V_{spring}/\partial l^2)|_{l_0}$ is the stretching modulus and $\kappa = k_b l_0$ is the RBC bending rigidity. $\alpha = 1340$ for RBCs [30], which has been roughly estimated by mimicking RBC stretching experiment [32]. The area constraint coefficient is set to $k_a = 37210 k_B T/D_r^2$.

Micro- and nano-particles are modeled by a collection of N_v^p particles, which are constrained to maintain a rigid configuration. Two shapes of particles are used in simulations including circular and elliptical particles. The particles are characterized by a size D_p , which corresponds to the diameter for circular particles and to the longest axis for elliptical particles.

Coupling between the fluid flow and cells/carriers is achieved through viscous friction [31] between cell vertices and the surrounding fluid particles, which is implemented via the DPD interactions F^D and F^R , see Appendix A. The strength γ of the dissipative force F^D for the interaction between a fluid particle and a membrane vertex is computed such that no-slip BCs are ensured. The derivation of γ is based on the idealized case of linear shear flow over a flat boundary with length L . The total shear force exerted by the fluid on the length L is equal to $L\eta\dot{\gamma}$, where η is the fluid's viscosity and $\dot{\gamma}$ is the local wall shear-rate. The same fluid force has to be also transmitted onto a discrete membrane having N_L vertices within the length L . The force on a single membrane vertex exerted by the sheared fluid can be found as $F_s = \int_{A_h} n g(r) F^D dA$ where n is the fluid number density, $g(r)$ is the radial distribution function of fluid particles with respect to the membrane particles, and A_h is the half circle volume of fluid above the membrane. Here, the total shear force on the length L is equal to $N_L F_s$. The equality of $N_L F_s = L\eta\dot{\gamma}$ results in an expression of the dissipative force coefficient in terms of the fluid density and viscosity, wall density N_L/L , and r_c . Under the assumption of linear shear flow the shear rate $\dot{\gamma}$ cancels out. This formulation results in satisfaction of the no-slip BCs for the linear shear flow over a flat membrane; however, it also serves as an excellent approximation for no-slip at the membrane surface. Note that conservative interactions between fluid and membrane particles are turned off, which implies that the radial distribution function is structureless, $g(r) = 1$.

size	$D_p = 0.3D_r$	$D_p = 0.63D_r$	$D_p = 0.15D_r$	$D_p = 0.04D_r$
N_v^p	20	20	15	10
$N_{W=20\mu\text{m}}$	6	6	20	100
$N_{W=10\mu\text{m}}$	6	/	14	/
$N_{W=40\mu\text{m}}$	12	/	30	/

Table 1: Carrier characteristics. N_v^p is the number of particles per carrier and N is the number of carriers in the system depending on the channel width and particle size.

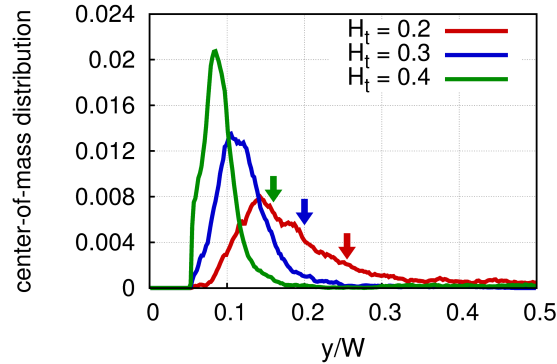


Fig. 3: Center-of-mass distributions of carriers for various H_t values at $\dot{\gamma}^* \approx 29.3$. Simulation results for circular particles with $D_p = 0.3D_r$ ($1.83\mu\text{m}$). The wall is at $y/W = 0$. The arrows indicate the boundary of the RBCFL for the different hematocrits, marked by corresponding colors.

2.2 Simulation setup and definitions

The simulation setup consists of a single slit-like channel with different widths $W = 10, 20,$ and $40\mu\text{m}$ and length $L = 19.5D_r$ independent of W . The channel is filled with fluid particles and with N suspended carriers and N_{RBC} RBCs. The number of RBCs is computed according to channel hematocrit, which corresponds to the area fraction of RBCs. The number of suspended particles for different simulations is provided in Table 1. An illustration of a typical simulation is shown in Fig. 2.

In the flow direction, periodic boundary conditions (BCs) are imposed, while in the other direction the suspension is confined by walls. The walls are modeled by frozen fluid particles with the same structure as the fluid, while the wall thickness is equal to r_c . Thus, the interactions of fluid particles with wall particles are the same as the interactions between fluid particles, and the interactions of suspended carriers and cells with the wall are identical to those with a suspending fluid. To prevent wall penetration, fluid particles as well as vertices of RBCs and carriers are subject to reflection at the fluid-solid interface. We employed bounce-back reflections, because they provide a better approximation for the no-slip boundary conditions in comparison to specular reflection of particles. To ensure that no-slip boundary conditions are strictly satisfied, we also add a tangential adaptive shear force [33] which acts on the fluid particles in a near-wall layer of a thickness $h_c = r_c$.

Blood flow is driven by a constant force applied to each solvent particle, which is equivalent to a prescribed pressure drop. To characterize the flow strength, we define a non-dimensional

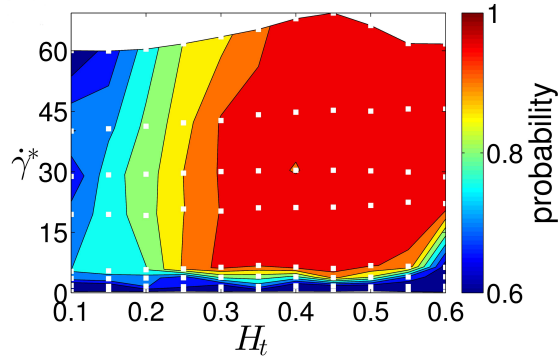


Fig. 4: Probability diagram of particle margination with respect to $\dot{\gamma}^*$ and H_t , where the margination probability is defined as a probability of a particle center-of-mass to be within the RBCFL. The white squares (\square) indicate the values of H_t and $\dot{\gamma}^*$ for which simulations have been performed.

shear rate as

$$\dot{\gamma}^* = \bar{\dot{\gamma}}\tau = \bar{\dot{\gamma}}\frac{\eta D_r^3}{\kappa}, \quad (4)$$

where $\bar{\dot{\gamma}} = \bar{v}/W$ is the average shear rate (or pseudo shear rate) and \bar{v} is the average flow velocity computed from the flow rate, while τ defines a characteristic RBC relaxation time.

To determine the RBC-free-layer (RBCFL) thickness, we measure the outer edge of the RBC core, which is similar to RBCFL measurements in experiments [34, 35]. The data is averaged for many RBC snapshots at different times.

3 Results

To study micro- and nano-particle margination for a wide range of conditions, we exploit the 2D blood flow model due to its numerical efficiency. However, our recent results [36] show that the 2D model is able to qualitatively reproduce the required blood flow characteristics and the particle margination effect in comparison with a realistic 3D model.

3.1 Particle margination

Carrier positions in blood flow sampled over time lead to particle distributions, which reflect the probability of a particle to be at a certain distance from the wall. Figure 3 shows several center-of-mass distributions of circular particles with $D_p = 0.3D_r$ ($1.83\mu\text{m}$) for several H_t values and $\dot{\gamma}^* \approx 29.3$. The RBC-free layer (RBCFL) thickness is depicted by small arrows. The distributions have been averaged over the halves of the channel due to symmetry. Figure 3 shows that the carriers migrate into the RBCFL and remain quasi-trapped there. With increasing H_t , the carriers marginate better, as indicated by the development of a strong peak in the distribution near the wall at $y/W = 0$, and the motion of the peak position towards the wall. This is due to a decrease in the RBCFL thickness leading to a smaller available space for the particles. This trend is in agreement with experimental observations [14] and simulations [37, 38] of margination of blood platelets, which have a comparable size.

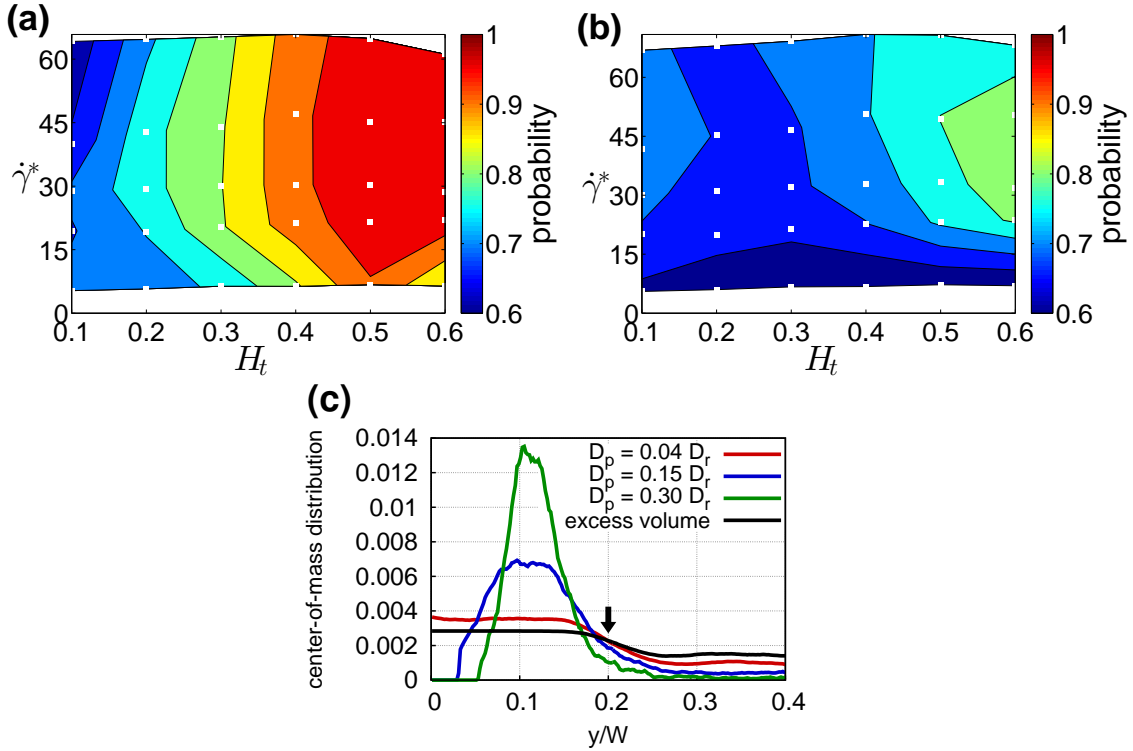


Fig. 5: Dependence of margination on particle size. Probability diagrams of particle margination for various H_t and $\dot{\gamma}^*$ values and for circular particles with the sizes (a) $D_p = 0.15 D_r$ ($0.91 \mu\text{m}$), (b) $D_p = 0.04 D_r$ ($0.25 \mu\text{m}$). The white squares (\square) indicate the values of H_t and $\dot{\gamma}^*$ for which simulation were performed. The margination probability is calculated based on the RBCFL thickness. (c) Distribution of particles with different sizes across the channel for $H_t = 0.3$ and $\dot{\gamma}^* \approx 29.3$. For small particles the distribution resembles the black solid curve computed as the blood-plasma volume. The arrow denotes position of the RBCFL boundary.

To quantify and compare particle margination for a wide range of flow and particle parameters, we define the margination probability as a fraction of particles whose center-of-mass is located within the near-wall layer of thickness δ . The choice of δ depends on the exact problem to be addressed, and several possibilities can be considered. To describe particle margination into the vicinity of a vessel wall, it is natural to select δ to be the RBCFL thickness. Figure 4 presents margination probability diagram of particles for a wide range of H_t and $\dot{\gamma}^*$ values. Particle margination strongly depends on H_t as well as on shear rate. At low H_t values, particle margination is expected to be weak, while at high H_t the margination might be also attenuated due to particle-RBC interactions near a wall. The latter effect has been described for a marginating white blood cell [30] and is expected to subside for particles substantially smaller than a RBC, i.e. of sub-micrometer size. A pronounced dependence of particle margination on shear rate is observed at low flow rates. In the limit of very small flow rates ($\dot{\gamma}^* \lesssim 1$), the RBC distribution should be nearly uniform, and therefore, the RBCFL and consequently particle margination should almost vanish. As the shear rate is increased, the RBCFL thickness grows rapidly, leading to a substantial increase in particle margination.

The simulated values of $\dot{\gamma}^*$ cover the range of flow rates characteristic for the venular part of microcirculation ($\bar{\dot{\gamma}} \lesssim 80 \text{ s}^{-1}$ for $W \approx 20 \mu\text{m}$), where it is estimated that $\dot{\gamma}^* \lesssim 77$, while in arteriolar part the flow rates are higher ($\bar{\dot{\gamma}} \gtrsim 110 \text{ s}^{-1}$ for $W \approx 20 \mu\text{m}$) [39, 40]. The

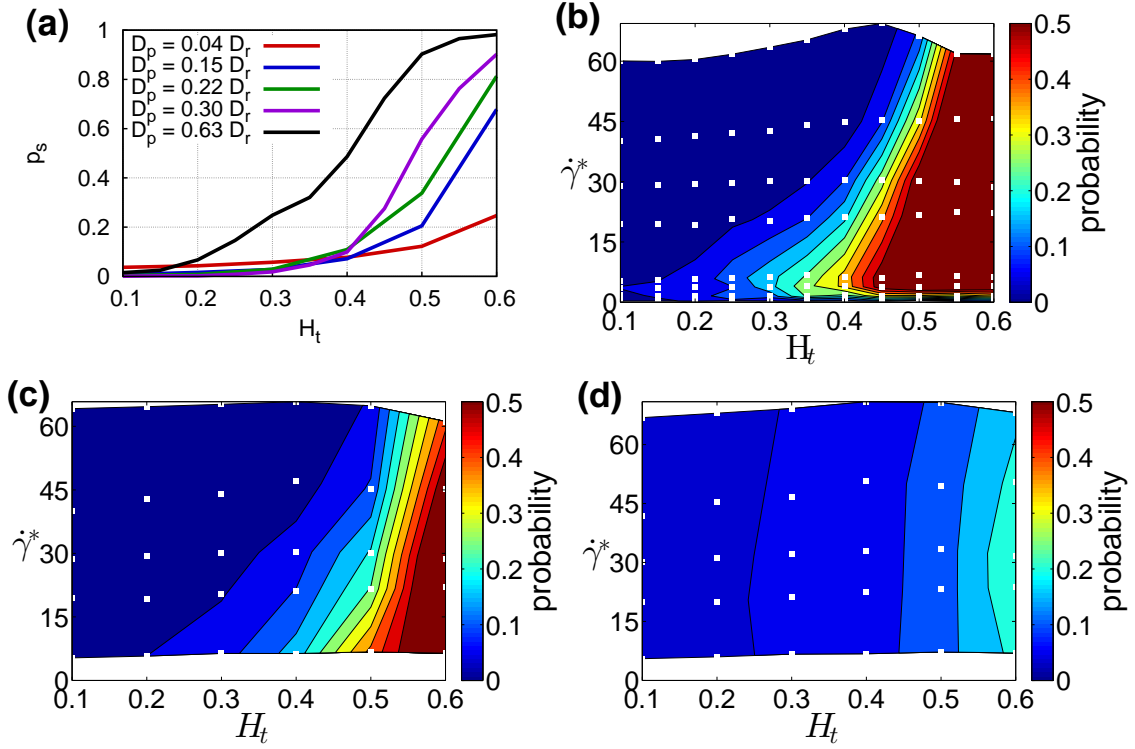


Fig. 6: Margination into a potential adhesion layer of thickness 200 nm. (a) Margination probability p_s . The curves correspond to different particle sizes, where $D_p = 0.63D_r$ ($3.84\mu\text{m}$) is for an elliptic particle and the other curves are for circular particles. Simulation results for $\dot{\gamma}^* \approx 29.3$. (b-d) Margination diagrams for (b) $D_p = 0.3D_r$ ($1.83\mu\text{m}$) (c) $D_p = 0.15D_r$ ($0.91\mu\text{m}$), and (d) $D_p = 0.04D_r$ ($0.25\mu\text{m}$).

considered range of shear rates is also relevant for tumor microvasculature, since blood flow velocities in tumors are much reduced in comparison to those under normal conditions, due to high geometric resistance and vessel permeability [41, 42]. Furthermore, the margination probability diagram in Fig. 4 shows that the strongest particle margination occurs in the range of $H_t = 0.2 - 0.6$. This region has a considerable overlap with the characteristic hematocrits in the body's microvascular networks in the range $H_t = 0.2 - 0.4$. A strong particle margination at high H_t values seems to be an advantage for drug delivery to tumors, since blood within tumor microvasculature is often subject to hemoconcentration due to plasma leakage [43].

3.2 Dependence of margination on particle size

The discussion above considered the margination of micron-size particles. There is also a strong interest in nano-carriers, with sizes starting from several nanometers. Figures 5(a),(b) show margination diagrams of particles with $D_p = 0.15D_r$ ($0.91\mu\text{m}$) and $D_p = 0.04D_r$ (250nm), respectively. The comparison of Figs. 5(a),(b) and Fig. 4 for $D_p = 0.3D_r$ ($1.83\mu\text{m}$) reveals that the region of high margination probability becomes smaller with decreasing particle size. To illustrate the reason for the reduction in margination probability with decreasing particle size, we present in Fig. 5(c) the distributions of particles with different sizes for $H_t = 0.3$ and $\dot{\gamma}^* \approx 29.3$. For large enough particles, we observe a pronounced peak in the distribution next to the wall due to their interactions with RBCs, since their size is comparable with the RBCFL

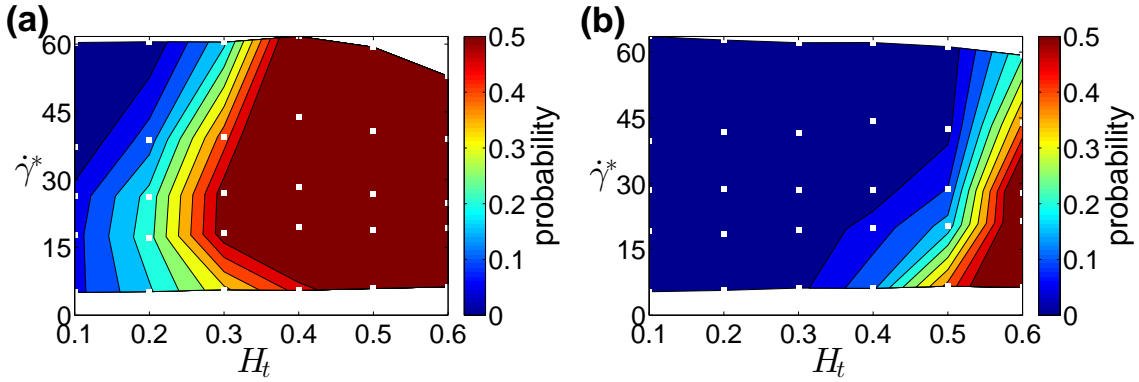


Fig. 7: Margination for different channel widths. Margination into the potential adhesion layer based on $\delta = 0.5D_p + 200\text{nm}$, for particles with size $D_p = 0.3D_r$ ($1.83\ \mu\text{m}$) and two channel widths (a) $W = 10\ \mu\text{m}$ and (b) $W = 40\ \mu\text{m}$.

thickness. Even though small particles are also margined, their distribution within the RBCFL is more uniform and their presence around the vessel center line is more probable than that for larger particles. Thus, the cumulative probability for a single particle to be within the RBCFL is lower for nano-carriers than that for micro-particles. Recent *in vivo* experiments [44] also support our numerical observations that particles with a size of about $1\ \mu\text{m}$ are located closer to the vessel wall than smaller nano-particles. Noteworthy is that the distribution of the smallest particles with $D_p = 0.04D_r$ closely approaches the distribution computed as the excess fluid volume of flowing RBCs. This indicates that the distribution of particles smaller in size than roughly $250\ \text{nm}$ can be well approximated by the distribution of the blood plasma, and therefore, their margination properties can be directly inferred from local H_t distributions.

To decide on a suitable particle size for efficient drug delivery, a number of different considerations have to be taken into account. A direct interpretation of probabilities in Figs. 4 and 5(a),(b) suggests that larger particle sizes are more favorable for drug delivery due to their better margination properties. To further support this proposition, we consider another definition for the margination probability based on $\delta = 0.5D_p + s$, which characterizes the fraction of carriers whose closest surface point is not further away from the wall than a distance s . We denote such a layer as "potential adhesion layer", since particle margination into a thin near-wall layer is a necessary precondition for adhesion. Even though the distance s is motivated by direct receptor-ligand interactions which occur within several nanometers, resolution restrictions in our mesoscale simulation approach do not allow the selection of smaller distances than approximately $s = 0.033D_r$, which corresponds to about $200\ \text{nm}$. Nevertheless, the distance of several hundred nanometers becomes relevant for particle-wall interactions in case of a carrier whose surface is decorated by tethered molecules [45]. Another definition for margination probability can also be based on a fixed layer thickness δ , thus it does not depend on H_t or on particle size. Figure 6(a) presents the margination probability into the potential adhesion layer (p_s) at $\dot{\gamma}^* \approx 29.3$. At very small H_t , the fraction of particles within the potential adhesion layer is small for all particle sizes; however, the smallest studied particles seem to be slightly more advantageous here. For the range of $H_t = 0.3 - 0.6$, Fig. 6(a) clearly shows that the fraction of large particles within the potential adhesion layer is much higher than that for small particles. The corresponding margination diagrams are shown in Figs. 6(b-d) and support the conclusion that large particles marginate better for all considered shear rates. This indicates that micro-carriers are likely to be better for drug delivery than sub-micron particles.

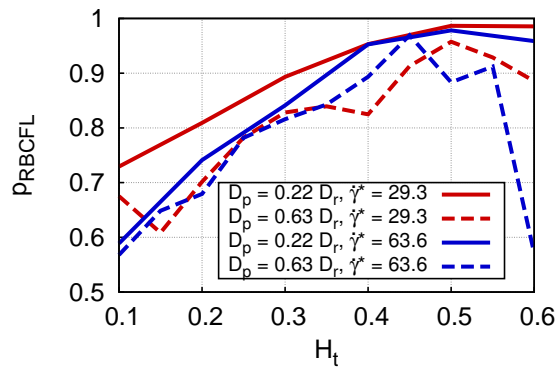


Fig. 8: *Dependence of margination on particle shape. Margination probabilities of ellipse-like particles (dashed lines) for various H_t and $\hat{\gamma}^*$ values in comparison to circular particles (solid lines) of the same area. The long axis of a 2D elliptic particle is $D_p = 0.63D_r$ ($3.84\mu\text{m}$) and the aspect ratio equals approximately 7. The margination probability is calculated based on the RBCFL thickness.*

3.3 Dependence of margination on vessel size

To elucidate the effect of vessel diameter, we performed a number of simulations for two additional channel widths ($W = 10\mu\text{m}$ and $40\mu\text{m}$) and two particle sizes ($D_p = 0.15D_r$ and $D_p = 0.3D_r$). The pronounced dependence of particle margination properties on channel width for the potential adhesion layer is illustrated by a comparison of Fig. 6(b) and Fig. 7. For particles with a size of $D_p = 0.3D_r$ ($1.83\mu\text{m}$), particle margination into the potential adhesion layer improves considerably as the channel size decreases due to the much smaller RBCFL thickness in narrow channels. Thus, particle adhesion is expected to be more efficient in small vessels (i.e., capillaries) than in large vessels (i.e., venules and arterioles). Similar observation is found for particles with $D_p = 0.15D_r$ ($0.91\mu\text{m}$) (not shown here). Furthermore, a reduction of margination into the potential adhesion layer with decreasing particle size is found for all channel sizes.

3.4 Dependence of margination on particle shape

Advances in micro- and nano-particle fabrication facilitate the production of carriers of various shapes, including spherical, prolate and oblate ellipsoidal, and rod-like shapes [4]. However, advantages of different particle shapes for drug delivery are still to be explored. Thus, we investigate the effect of shape on the margination properties in blood flow. Figure 8 displays results of simulations for the margination probability (based on the RBCFL) of elliptic particles under various blood flow conditions in comparison to circular particles. The ellipse has an aspect ratio of about 7 and the longest diameter is $D_p = 0.63D_r$ ($3.84\mu\text{m}$); the enclosed area corresponds to the area of a circle with diameter $D_p = 0.22D_r$ ($1.35\mu\text{m}$). The plot indicates that margination of elliptic particles is slightly worse than that of circular particles. From these data we can also conclude that margination of the elliptic particles with a smaller aspect ratio than 7 is similar to that presented in Fig. 8. However, since the largest diameter of the ellipse is larger than that of a circle with the same area, its margination into the potential adhesion layer, which is defined as a probability of a particle to be within a near-wall layer of thickness $\delta = 0.5D_p + 200\text{ nm}$, appears to be considerably larger for ellipses than that for the corresponding

circle (see Fig. 6). Recent theoretical [26, 27] and experimental [24, 25] studies also suggest that ellipsoidal particles possess better adhesion properties than spheres due to a larger contact area for adhesion interactions. In conclusion, the current knowledge about adhesion of ellipsoidal particles and our simulation results on margination suggest that ellipsoidal particles are very likely a better choice for drug delivery than spherical particles.

4 Discussion and conclusions

Particle margination in blood flow depends on particle size and shape, hematocrit, vessel size, and flow rate. Margination of circular and elliptical particles increases with increasing hematocrit, while their margination properties appear to be rather similar, where a circle marginates slightly more efficiently than an ellipse. The presented diagrams show that larger particles have a higher margination probability in comparison to the smaller ones. Moreover, the distribution of very small particles with a diameter smaller than approximately 250 nm is well represented by the blood plasma volume of RBCs. Margination of particles into the potential adhesion layer is found to be more pronounced in small vessels, indicating that particle adhesion is likely to occur more often in capillaries than in arterioles and venules.

The simulation results are in good qualitative agreement with several experimental observations [13, 14, 21, 24, 25, 44]. For example, margination of micro-particles has been observed to be more efficient than that of nano-particles in recent *in vivo* experiments [44]. However, a detailed quantitative comparison is still difficult due to two reasons. On the one hand, the simulation results are obtained for 2D systems, which provide interesting insights into the relevant mechanisms, but have limited power for quantitative predictions for 3D systems. On the other hand, experimental data on particle margination in blood flow [13, 44] are very scarce and most of the available experimental investigations (e.g., Refs. [21, 24, 25]) focus on carrier adhesion. Even though margination is a necessary pre-condition for particle adhesion to vessel walls, particle margination and adhesion are not equivalent, since carrier adhesion may also depend on other factors (e.g., specific targets, the receptor/ligand density and distribution).

Clearly, the size and shape of drug carriers are important parameters not only for margination, but also for their adhesion and further transport through biological barriers (e.g., internalization). Our simulations suggest that elliptical particles are expected to adhere more efficiently than circular carriers due to a larger surface for adhesive interactions; however, this needs to be systematically investigated. Further requirements for efficient drug delivery include particle transport through vessel walls, interstitial space, and cell membranes. For instance, particle internalization by endothelial cells and intracellular trafficking have been shown to be most efficient for spherical sub-micron particles, rather than for micron-size carriers with an ellipsoidal shape [8]. This observation points in the direction of smaller carriers to be most efficient for internalization. As a consequence, the concept of multi-stage drug-delivery carriers [1, 5], where a larger micro-particle incorporates a number of small nano-carriers, seems to be very promising. In this way, margination and carrier delivery or adhesion to a specific target within the microvasculature could be achieved using micro-particles, which would then be followed by the release of nano-particles into the tissue. In conclusion, tackling various drug-delivery challenges is a complex issue; its resolution requires an inter-disciplinary effort including *in vitro* and *in vivo* experiments and realistic numerical simulations.

	m	a	γ	r_c	s	n	$k_B T$	η
$\dot{\gamma}^* \leq 20$	1	40	10	1.5	0.3	5	1	72.2
$\dot{\gamma}^* > 20$	1	40	20	1.5	0.3	5	1	144.4

Table 2: DPD fluid parameters used in simulations. m is the mass of a fluid particle, a and γ are the conservative and dissipative force coefficients, respectively. r_c is the interaction cutoff radius, k is an exponent for the random-force weight function, n is the number density of fluid particles, $k_B T$ is the energy unit with k_B being the Boltzmann constant and T temperature, and η is the fluid's dynamic viscosity. $\dot{\gamma}^*$ is the non-dimensional shear rate defined in the main text.

Appendices

A Dissipative particle dynamics

Dissipative particle dynamics (DPD) [28, 29] is a mesoscopic particle-based method, where each particle represents a *molecular cluster* rather than an individual atom, and can be thought of as a soft lump of fluid. The DPD system consists of N point particles of mass m_i , position \mathbf{r}_i and velocity \mathbf{v}_i . DPD particles interact through three forces: conservative (\mathbf{F}_{ij}^C), dissipative (\mathbf{F}_{ij}^D), and random (\mathbf{F}_{ij}^R) forces given by

$$\mathbf{F}_{ij}^C = F_{ij}^C(r_{ij})\hat{\mathbf{r}}_{ij}, \quad \mathbf{F}_{ij}^D = -\gamma\omega^D(r_{ij})(\mathbf{v}_{ij} \cdot \hat{\mathbf{r}}_{ij})\hat{\mathbf{r}}_{ij}, \quad \mathbf{F}_{ij}^R = \sigma\omega^R(r_{ij})\frac{\xi_{ij}}{\sqrt{dt}}\hat{\mathbf{r}}_{ij}, \quad (5)$$

where $\hat{\mathbf{r}}_{ij} = \mathbf{r}_{ij}/r_{ij}$, and $\mathbf{v}_{ij} = \mathbf{v}_i - \mathbf{v}_j$. The coefficients γ and σ define the strength of dissipative and random forces, respectively. In addition, ω^D and ω^R are weight functions, and ξ_{ij} is a normally distributed random variable with zero mean, unit variance, and $\xi_{ij} = \xi_{ji}$. All forces are truncated beyond the cutoff radius r_c . The conservative force is given by

$$F_{ij}^C(r_{ij}) = a_{ij}(1 - r_{ij}/r_c) \quad \text{for } r_{ij} \leq r_c, \quad (6)$$

where a_{ij} is the conservative force coefficient between particles i and j . The random and dissipative forces form a thermostat and must satisfy the fluctuation-dissipation theorem in order for the DPD system to maintain equilibrium temperature T [29]. This leads to

$$\omega^D(r_{ij}) = [\omega^R(r_{ij})]^2, \quad \sigma^2 = 2\gamma k_B T, \quad (7)$$

where k_B is the Boltzmann constant. The choice for the weight functions is as follows

$$\omega^R(r_{ij}) = (1 - r_{ij}/r_c)^k \quad \text{for } r_{ij} \leq r_c, \quad (8)$$

where k is an exponent. The time evolution of velocities and positions of particles is determined by the Newton's second law of motion

$$d\mathbf{r}_i = \mathbf{v}_i dt, \quad d\mathbf{v}_i = \frac{1}{m_i} \sum_{j \neq i} (\mathbf{F}_{ij}^C + \mathbf{F}_{ij}^D + \mathbf{F}_{ij}^R) dt. \quad (9)$$

The above equations of motion are integrated using the velocity-Verlet algorithm [46]. The DPD fluid parameters used in simulations are given in Table 2.

References

- [1] M. Ferrari, *Nat. Rev. Cancer* **5**, 161 (2005).
- [2] R. K. Jain and T. Stylianopoulos, *Nat. Rev. Clin. Oncol.* **7**, 653 (2010).
- [3] R. Duncan, *Nat. Rev. Cancer* **6**, 688 (2006).
- [4] J. P. Rolland, B. W. Maynor, L. E. Euliss, A. E. Exner, G. M. Denison, and J. M. DeSimone, *J. Am. Chem. Soc.* **127**, 10096 (2005).
- [5] E. Blanco, A. Hsiao, A. P. Mann, M. G. Landry, F. Meric-Bernstam, and M. Ferrari, *Cancer Sci.* **102**, 1247 (2011).
- [6] W. R. Sanhai, J. H. Sakamoto, R. Canady, and M. Ferrari, *Nat. Nanotechnol.* **3**, 242 (2008).
- [7] R. K. Jain, *J. Natl. Cancer Inst.* **81**, 570 (1989).
- [8] S. Muro, C. Garnacho, J. A. Champion, J. Leferovich, C. Gajewski, E. H. Schuchman, S. Mitragotri, and V. R. Muzykantov, *Mol. Ther.* **16**, 1450 (2008).
- [9] R. B. Huang, S. Mocherla, M. J. Heslinga, P. Charoenphol, and O. Eniola-Adefeso, *Mol. Membr. Biol.* **27**, 312 (2010).
- [10] B.-S. Ding, T. Dziubla, V. V. Shuvaev, S. Muro, and V. R. Muzykantov, *Mol. Interv.* **6**, 98 (2006).
- [11] U. Bagge and R. Karlsson, *Microvasc. Res.* **20**, 92 (1980).
- [12] H. L. Goldsmith and S. Spain, *Microvasc. Res.* **27**, 204 (1984).
- [13] G. J. Tangelder, H. C. Teirlinck, D. W. Slaaf, and R. S. Reneman, *Am. J. Physiol.* **248**, H318 (1985).
- [14] A. W. Tilles and E. C. Eckstein, *Microvasc. Res.* **33**, 211 (1987).
- [15] E. C. Eckstein, A. W. Tilles, and F. J. Millero III, *Microvasc. Res.* **36**, 31 (1988).
- [16] I. Cantat and C. Misbah, *Phys. Rev. Lett.* **83**, 880 (1999).
- [17] M. Abkarian, C. Lartigue, and A. Viallat, *Phys. Rev. Lett.* **88**, 068103 (2002).
- [18] A. Kumar and M. D. Graham, *Phys. Rev. Lett.* **109**, 108102 (2012).
- [19] J. D. Slack, M. Kanke, G. H. Simmons, and P. P. DeLuca, *J. Pharm. Sci.* **70**, 660 (1981).
- [20] M. Herant, V. Heinrich, and M. Dembo, *J. Cell Sci.* **119**, 1903 (2006).
- [21] K. Namdee, A. J. Thompson, P. Charoenphol, and O. Eniola-Adefeso, *Langmuir* **29**, 2530 (2013).
- [22] D. C. Litzinger, A. M. J. Buiting, N. van Rooijen, and L. Huang, *Biochim. Biophys. Acta* **1190**, 99 (1994).

- [23] W. H. De Jong, W. I. Hagens, P. Krystek, M. C. Burger, A. J. A. M. Sips, and R. E. Geertsma, *Biomaterials* **29**, 1912 (2008).
- [24] F. Gentile, C. Chiappini, D. Fine, R. C. Bhavane, M. S. Peluccio, M. M.-C. Cheng, X. Liu, M. Ferrari, and P. Decuzzi, *J. Biomech.* **41**, 2312 (2008).
- [25] A. J. Thompson, E. M. Mastria, and O. Eniola-Adefeso, *Biomaterials* **34**, 5863 (2013).
- [26] P. Decuzzi and M. Ferrari, *Biomaterials* **27**, 5307 (2006).
- [27] S. Dasgupta, T. Auth, and G. Gompper, *Soft Matter* **9**, 5473 (2013).
- [28] P. J. Hoogerbrugge and J. M. V. A. Koelman, *Europhys. Lett.* **19**, 155 (1992).
- [29] P. Español and P. Warren, *Europhys. Lett.* **30**, 191 (1995).
- [30] D. A. Fedosov, J. Fornleitner, and G. Gompper, *Phys. Rev. Lett.* **108**, 028104 (2012).
- [31] D. A. Fedosov, B. Caswell, and G. E. Karniadakis, *Biophys. J.* **98**, 2215 (2010).
- [32] S. Suresh, J. Spatz, J. P. Mills, A. Micoulet, M. Dao, C. T. Lim, M. Beil, and T. Seufferlein, *Acta Biomaterialia* **1**, 15 (2005).
- [33] D. A. Fedosov and G. E. Karniadakis, *J. Comp. Phys.* **228**, 1157 (2009).
- [34] N. Maeda, Y. Suzuki, J. Tanaka, and N. Tateishi, *Am. J. Physiol.* **271**, H2454 (1996).
- [35] S. Kim, R. L. Kong, A. S. Popel, M. Intaglietta, and P. C. Johnson, *Am. J. Physiol.* **293**, H1526 (2007).
- [36] K. Müller, D. A. Fedosov, and G. Gompper, *Sci. Rep.* **4**, 4871 (2014).
- [37] L. Crowl and A. L. Fogelson, *J. Fluid Mech.* **676**, 348 (2011).
- [38] D. A. Reasor Jr, M. Mehrabadi, D. N. Ku, and C. K. Aidun, *Ann. Biomed. Eng.* **41**, 238 (2013).
- [39] A. S. Popel and P. C. Johnson, *Annu. Rev. Fluid Mech.* **37**, 43 (2005).
- [40] A. R. Pries, T. W. Secomb, and P. Gaetgens, *Am. J. Physiol.* **269**, H1713 (1995).
- [41] R. K. Jain, *Cancer Res.* **48**, 2641 (1988).
- [42] F. Yuan, H. A. Salehi, Y. Boucher, U. S. Vasthare, R. F. Tuma, and R. K. Jain, *Cancer Res.* **54**, 4564 (1994).
- [43] E. M. Sevick and R. K. Jain, *Cancer Res.* **49**, 3513 (1989).
- [44] T.-R. Lee, M. Choi, A. M. Kopacz, S.-H. Yun, W. K. Liu, and P. Decuzzi, *Sci. Rep.* **3**, 2079 (2013).
- [45] N. W. Moore and T. L. Kuhl, *Biophys. J.* **91**, 1675 (2006).
- [46] M. P. Allen and D. J. Tildesley, *Computer simulation of liquids* (Clarendon Press, New York, 1991).